

# Investigating biomineralization using synchrotron based X-ray computed microtomography

Ryan Armstrong<sup>1,2</sup> and Jonathan Ajo-Franklin<sup>2</sup>

Received 31 January 2011; revised 16 March 2011; accepted 25 March 2011; published 28 April 2011.

[1] This work presents the results of a study where synchrotron based x-ray computed microtomography (CMT) was used to investigate changes in pore morphology during calcium carbonate biomineralization. We simultaneously examine changes in pore microstructure and bulk permeability within glass bead columns during biogenic  $\text{CaCO}_3$  precipitation induced by *Sporosarcina pasteurii*. We observe a three order of magnitude reduction in permeability over relatively short time-scales (~60 hrs) during the carbonate precipitation process. The resulting precipitates were a microporous composite of spherical and cubic  $\text{CaCO}_3$  precipitates. CMT images taken during precipitation were analyzed for effective pore radii, effective throat radii, and other pore-scale characteristics using 3DMA-ROCK. The Kozeny-Carman relation provided a poor fit to the raw permeability data, however, once this function was augmented with geometric information extracted from CMT imagery a better fit was provided suggesting that pore geometry should be considered temporally variable when modeling permeability change during biomineralization. **Citation:** Armstrong, R., and J. Ajo-Franklin (2011), Investigating biomineralization using synchrotron based X-ray computed microtomography, *Geophys. Res. Lett.*, 38, L08406, doi:10.1029/2011GL046916.

## 1. Introduction

[2] Biomineralization is a natural subsurface process that can dramatically alter the physical properties of porous media. In particular, porosity and permeability changes, attributed to biologically assisted  $\text{CaCO}_3$  precipitation, can have a direct effect on fluid flow and transport properties [Whiffin *et al.*, 2007]. A key factor relevant to permeability alteration is the characteristic pattern of precipitation with respect to the granular matrix, i.e., are precipitates localized in pore throats, pore bodies, or on grain surfaces? Since effective medium models describing permeability [e.g., Carrier, 2003] and elastic properties [Dvorkin *et al.*, 1999] are dependent on such patterns, the appropriate choice of a scenario or trajectory between scenarios (i.e., where is precipitation localized and how does localization change temporally) is a key step in building a quantitative understanding of the effects of biomineralization.

[3] We selected *Sporosarcina pasteurii* as our model organism for studying the mineralization process, a prevalent aerobic, rod-shaped, motile, soil microbe with a very

active urease enzyme [Whiffin *et al.*, 2007]. Hydrolysis of urea by the urease enzyme generates carbon dioxide and ammonia  $\{\text{CO}(\text{NH}_2)_2 + \text{H}_2\text{O} \rightarrow 2\text{NH}_3 + \text{CO}_2\}$ , causing an increase in pH  $\{2\text{NH}_3 + 2\text{H}_2\text{O} \rightleftharpoons 2\text{NH}_4^+ + 2\text{OH}^-\}$ . Within this alkaline environment carbonate ions form  $\{\text{CO}_2 + 2\text{OH}^- \rightleftharpoons \text{CO}_3^{2-} + \text{H}_2\text{O}\}$  and precipitation of calcium carbonate is favored  $\{\text{CO}_3^{2-} + \text{Ca}^{2+} \rightleftharpoons \text{CaCO}_3(\text{s})\}$ , [Stocks-Fischer *et al.*, 1999].

[4] One of the simplest permeability models is the Kozeny-Carman (KC) model which attempts to describe permeability in terms of porosity starting from first principles [Carrier, 2003]. The KC function often fails to represent empirical data, however, this type of relationship is vital for the design and modeling of many engineered processes (e.g., geological carbon storage and hydrocarbon recovery).

[5] A complete derivation of the KC functions (equations (1) and (2)) used herein is presented by [Costa, 2006]. Permeability can be calculated using:

$$\kappa = c(R^2/8)(\theta/\tau) \quad (1)$$

where,  $R$  is effective radius,  $\tau$  is tortuosity, and  $\theta$  is porosity. However,  $R$  and  $\tau$  are hard to measure/define, thus the concept of hydraulic radius is usually defined and incorporated into equation (1) which gives the following formula:

$$\kappa = C_{kc}(\theta^3)/(1 - \theta)^2 \quad (2)$$

where,  $C_{kc}$  is an empirical constant. Equation (2) is essentially the classical KC function and is the starting point of our analysis. Average effective throat radius measured from CMT imagery is incorporated into equation (1) and fitted to the empirical data.

## 2. Methods

### 2.1. Experimental Setup

[6] A schematic of the flow-through bioreactor ( $L = 12$  mm,  $ID = 8$  mm) is provided in Figure S1 of the auxiliary material.<sup>1</sup> The reactor was equipped with internal pressure ports and separate flow lines for urea media and calcium chloride to prevent precipitation outside the column. The column was packed with 600  $\mu\text{m}$  diameter soda lime glass beads.

### 2.2. Cementation Treatment

[7] *S. pasteurii* (ATCC 6453) was grown to late exponential stage (~18 hours) in batch culture. Prior to inoculation, microbes were rinsed with urea media (20.0 g  $\text{CO}(\text{NH}_2)_2$ , 10.0 g  $\text{NH}_4\text{Cl}$ , 2.1 g  $\text{NaHCO}_3$ , 3.0 g Difco Nutrient Broth, total volume 1.0 L DI  $\text{H}_2\text{O}$ ) by three rounds of centrifugation

<sup>1</sup>School of Chemical, Biological and Environmental Engineering, Oregon State University, Corvallis, Oregon, USA.

<sup>2</sup>Earth Science Division, Lawrence Berkeley National Laboratory, Berkeley, California, USA.

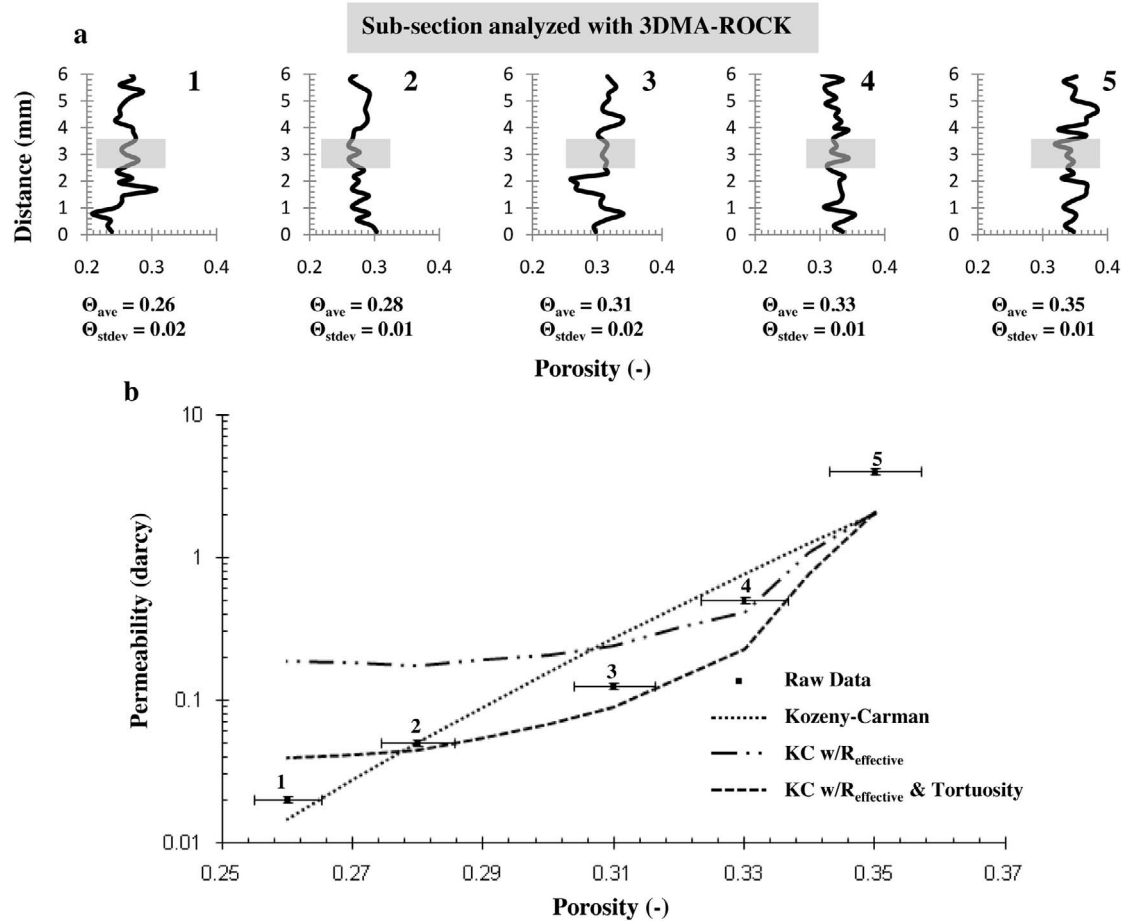


**Figure 1.** (a) The porosity distributions between the pressure transducer ports for each column labeled 1 through 5. (b) The porosity-permeability data along with the KC curves. Each data point in Figure 1b is labeled 1 through 5 and the given porosity value corresponds to the mean porosity value calculated from the porosity distributions shown in Figure 1a. The mean porosity and standard deviation for each column is reported directly below its corresponding porosity distribution graph.

and resuspension in fresh urea media followed by pH adjustment to 6.5 with 1 N HCl. Columns were inoculated with approximately  $10^{10}$  cells/ml and flow was discontinued for 4 hours allowing the microbes to revive and increase pore water pH. After the stagnant period urea media was pumped at 1.00 ml/hr and  $\text{CaCl}_2$  (100 g/L) at 0.067 ml/hr (using a Harvard '33' syringe pump) giving a total Darcy velocity of  $5.9\text{E-}6$  m/hr and a 20 mM calcium concentration.

### 2.3. Computed Microtomography

[8] Imaging was performed at Beamline 8.3.2 at the Advanced Light Source (ALS), Lawrence Berkeley National Laboratory. Projections were acquired at  $4.5 \mu\text{m}/\text{pixel}$  resolution with a monochromatic energy of 30 KeV and flow was discontinued during each scan which took ~40 minutes.

### 2.4. Porosity and Permeability Measurements

[9] Permeability was measured under fixed flux conditions using a differential pressure transducer (Validyne, Model P55D, 1 PSI differential). CMT volumes were segmented into solid and fluid phases for porosity calculations. After applying a median filter ( $3 \times 3 \times 3$  kernel) it was determined that a simple threshold was sufficient to segment the solid (glass and calcium carbonate) and liquid phases (image histograms are provided in Figure S2).

### 2.5. Image Analysis Using 3DMA-ROCK

[10] Segmented volumes were imported into 3DMA-ROCK (3DMA) for medial axis and pore body/throat construction. When referring to the 3DMA data, effective pore radii is the radius of a sphere of equivalent volume and effective throat radii is the radius of a circle of equivalent area. For more detailed information on the algorithms used within 3DMA refer to the manuscript by [Prodanović *et al.*, 2007, and references therein]. An example medial axis and the corresponding pore throats is provided in Figure S3.

[11] Since medial axis and pore body/throat construction can be time intensive the analyzed image volume was restricted to a volume that could be processed within a reasonable amount of time. A volume of  $25 \text{ mm}^3$  was found reasonable and took ~40 hours on a 64 GB RAM, dual quad core Xeon X5355 2.66 GHz processor platform to process.

## 3. Results

[12] In total, 5 columns were analyzed, 1 column was a clean bead pack used to characterize the system prior to precipitation and the other 4 columns contained bioprecipitates. Once a column was imaged with CMT the experiment was ceased. This type of terminal sampling was required since preliminary experiments showed that x-ray exposure

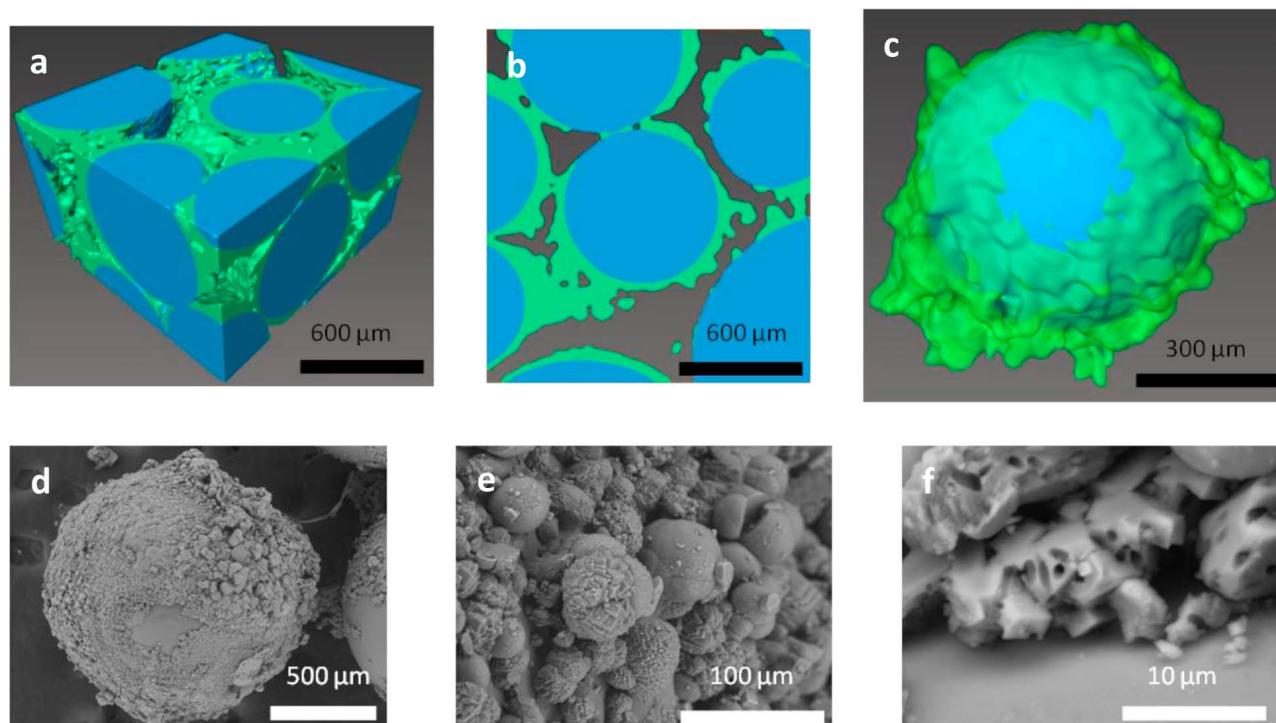


**Figure 2.** (a–c) CMT images (blue = glass, green =  $\text{CaCO}_3$ ). (d–f) SEM images.

during a scan ( $2.2 \times 10^{11}$  photons/(s mm<sup>2</sup>), ~40 minutes) killed 99 out of 100 microbes.

[13] Porosity and permeability data for the 5 columns which range in porosity from 0.35 to 0.26 and had measured permeabilities ranging from 4 D to 20 mD are shown in Figure 1. The clean glass bead pack is labeled as 5 in Figure 1. For the column with the smallest porosity change labeled as 4 in Figure 1 the cementation treatment took ~1 day, the two columns labeled 3 and 2 in Figure 1 with intermediate porosity changes were treated for ~2 days, while the column with the greatest porosity change labeled 1 in Figure 1 was treated for ~3 days. The porosity profile over the vertical axis for each column is shown in Figure 1a. The average porosity versus measured permeability is shown in Figure 1b and shows a dramatic decrease in permeability from the starting point at  $\theta = 0.35$  (5) for a clean glass bead pack to  $\theta = 0.26$  (1) for a completely cemented packing. Initially the KC function ( $\kappa = C_{kc}(\theta^b)$ ) was fitted to the raw data in log space with  $C_{kc} = 7.0\text{E-}7$  and  $b = 16.54$  providing the best fit possible, however, the variable  $b$  deviates far from realistic  $b$  values derived from KC theory (Figure 1b). More information on curve fitting and quality-of-fit statistics are provided in Figures S6 and S7.

[14] The average effective pore body radius, average effective pore throat radius, and permeability for each column are shown in Figure S4. The average effective pore body and average effective throat radii decrease during precipitation. Because a fixed water flux was imposed by pumping, mean pore velocity and pore pressure significantly increase within the highly precipitated channel. Washout of precipitates was observed in the lower permeability columns and was likely due to this increased pore velocity; however, no data is available to quantify the amount of precipitate that was washed out.

[15] As shown in the CMT images provided in Figures 2a–2c calcium carbonate appears to precipitate on the glass bead

surface and extend outward into the pore space. This type of arrangement is indicative of the coupling of mass transfer and growth kinetics where calcium must diffuse from the bulk pore-space to the reactive surface (Figure 2c) where precipitation occurs and extends the surface outward into the pore space. However, this arrangement could also be attributed to inconsistent local cell densities causing a variation in precipitation rate. Either way, this effectively causes some regions to develop “peaks” where precipitation is favored (i.e., accelerated). These “peak” regions extend into the pore space dividing up what was a single pore into multiple pores (as identified by 3DMA, Figure S4) and in some locations enough precipitation occurs that adjacent beads become cemented together.

[16] To better represent the permeability data with the KC function, average effective throat radius ( $R_{\text{effective}}$ ) data were used to supplement equation (1). For porosity values where  $R_{\text{effective}}$  values were not available, a linear interpolation between measured  $R_{\text{effective}}$  values was used. Tortuosity was held constant at 1.5 (average theoretical tortuosity for a clean glass bead pack) and the KC function with  $R_{\text{effective}}$  was fit to the raw data, results (Figure 1b) show a better fit, however, this function still failed to represent the empirical data (fitting parameter,  $C = 5.3$ ). In a third attempt tortuosity was used as a fitting parameter and allowed to change for each porosity value. The KC function with  $R_{\text{effective}}$  and tortuosity included provided the best fit (Figure 1b, fitting parameters,  $C = 5.3$  &  $\tau = 1.5$  to  $7.2$ ). However, this approach still did not completely represent the empirical data and a tortuosity value of 7.2 seems unrealistic. Most likely, in the case of biomineralization, the KC function is too simple to properly represent the complex porosity-permeability relationship. However, two reasonable propositions that could explain our inability to predict the empirical data with the KC function

must be addressed, which are either (1) sub-CMT resolution precipitate morphology is significantly reducing permeability or (2) biofilm formation which is not visible with CMT is reducing permeability.

[17] To address the first proposition, backscattered electron SEM images (Hitachi TM-1000, Figures 2d–2f) of the precipitates were acquired; the excavated samples were drained and air dried at 30°C for 48 hours before being mounted with carbon tape and imaged in low vacuum conditions to mitigate charging artifacts. SEM images show that calcium carbonate precipitates are an assemblage of spherical and cubic precipitates that are micro-porous. Figure 2 suggests that when modeling biomineralization the precipitate should not be considered a solid phase, and thus, its internal micro-porosity should be considered. However, it is reasonable to suggest that micro-porosity would not dramatically affect permeability since the pores appear too small for bulk advective transport. Figures S8 and S9 provide additional details concerning the mixed precipitate morphology and precipitate composition. As found by *Fredrich et al.* [2006], the relationship between porosity and permeability depends on effective porosity and not the disconnected microporosity that exists at near sub-CMT resolution. Overall, micro-porosity is more likely an important parameter when considering reactivity, structural soil mechanics, and the geophysical signature of biomineralization.

[18] A second possibility is clogging due to accumulated non-mineral biological products. Microbes and exopolymeric substances have very similar x-ray attenuation coefficient as water and are not readily seen with CMT, thus any additional clogging due to bioaccumulation would not have been accounted for. However, recent confocal laser scanning microscopy images of *S. pasteurii* reported by [Schultz et al., 2011] show that this particular organism forms a sparse biofilm. Nevertheless, permeability reduction due to biofilm formation cannot be ruled out, at this point.

#### 4. Conclusion

[19] Our results demonstrate that traditional KC models are not sufficient for predicting the porosity-permeability relationship observed during biomineralization and geometric information from CMT images were needed to supplement the KC function. A similar conclusion was reached by *Chen et al.* [2008], where inorganic colloid deposition within an initially simple porous media produced sufficient internal complexity, such that, the KC function could not provide a good fit. Pore morphology dramatically changed as a result of precipitation, increasing the number of pore bodies (and throats) and decreasing the effective radii of pore throats and pore bodies. The discrepancy with the simple KC function suggests that field scale reactive transport models will require more sophisticated porosity/permeability models

to effectively capture changes in transport properties generated during bioremediation or biologically-enhanced CO<sub>2</sub> sequestration. Overall, biomineralized CaCO<sub>3</sub> substantially reduced permeability. When modeling this reduction, porosity, effective throat radius, tortuosity, and the biofilm phase should be considered to vary both spatially and temporally.

[20] **Acknowledgments.** Primary support was provided by the U.S. DOE Biological and Environmental Research Program (contract DE-AC02-05CH11231) through the LBNL Sustainable Systems Scientific Focus Area. Secondary support for J.A-F, provided by the Center for Nano-scale Control of Geologic CO<sub>2</sub>, an Energy Frontier Research Center, funded by U.S. DOE, Office of Basic Energy Sciences (contract DE-AC02-05CH11231). We also thank Jamie Nasiatka (ALS, BL8.3.2) for flowcell design, Maša Prodanović (UT Austin) for providing 3DMA, Qianoa Hu for SEM imaging assistance, and Dorte Wildenschild (OSU) for computing support. CMT work was performed with the assistance of Alastair MacDowell at the Advanced Light Source, Beamline 8.3.2, which is supported by the Office of Science, Office of Basic Energy Sciences, of the U.S. DOE (contract DE-AC02-05CH11231). Microbiological work was performed with the assistance of Caroline Ajo-Franklin as a User project at the Biological Nanostructure Facility within the Molecular Foundry (LBNL) which is supported by the Office of Science, Office of Basic Energy Sciences, of the U.S. DOE (contract DE-AC02-05CH11231).

[21] The Editor thanks Aaron Packman and anonymous reviewer for their assistance in evaluation this paper.

#### References

- Carrier, D. (2003), Goodbye, Hazen; Hello, Kozeny-Carman, *J. Geotech. Geoenviron. Eng.*, 129, 1054, doi:10.1061/(ASCE)1090-0241(2003)129:11(1054).
- Chen, C., A. I. Packman, and J.-F. Gaillard (2008), Pore-scale analysis of permeability reduction resulting from colloid deposition, *Geophys. Res. Lett.*, 35, L07404, doi:10.1029/2007GL033077.
- Costa, A. (2006), Permeability-porosity relationship: A reexamination of the Kozeny-Carman equation based on a fractal pore-space geometry assumption, *Geophys. Res. Lett.*, 33, L02318, doi:10.1029/2005GL025134.
- Dvorkin, J., J. Berryman, and A. Nur (1999), Elastic moduli of cemented sphere packs, *Mech. Mater.*, 31, 461–469, doi:10.1016/S0167-6636(99)00009-5.
- Fredrich, J. T., A. A. DiGiovanni, and D. R. Noble (2006), Predicting macroscopic transport properties using microscopic image data, *J. Geophys. Res.*, 111, B03201, doi:10.1029/2005JB003774.
- Prodanović, M., W. Lindquist, and R. Seright (2007), 3D image-based characterization of fluid displacement in Berea core, *Adv. Water Resour.*, 30, 214–226, doi:10.1016/j.advwatres.2005.05.015.
- Schultz, L., B. Pitts, A. Mitchell, A. Cunningham, and R. Gerlach (2011), Imaging biologically-induced mineralization in fully hydrated flow systems, *Microsc. Today*, doi:10.1017/S1551929510001239.
- Stocks-Fischer, S., J. Galinat, and S. Bang (1999), Microbiological precipitation of CaCO<sub>3</sub>, *Soil Biol. Biochem.*, 31, 1563–1571, doi:10.1016/S0038-0717(99)00082-6.
- Whiffin, V., L. van Paassen, and M. Harkes (2007), Microbial carbonate precipitation as a soil improvement technique, *Geomicrobiol. J.*, 24, doi:10.1080/01490450701436505.

J. Ajo-Franklin, Earth Science Division, Lawrence Berkeley National Laboratory, 1 Cyclotron Rd., Berkeley, CA 94720, USA.

R. Armstrong, School of Chemical, Biological and Environmental Engineering, Oregon State University, 103 Gleeson Hall, Corvallis, OR 97331, USA. (armstror@onid.orst.edu)